Efficient infrared-light-driven photothermal CO_2 reduction over MOF-derived defective Ni/TiO_2

Qiang Li [a,b,e], Yanxia Gao [a,b,e], Meng Zhang [a,b,e], Hui Gao [a,b,e], Jing Chen [c,d,e], Hongpeng Jia [a,b,e,**]

[a] *Xiamen Key Laboratory of Materials for Gaseous Pollutant Control, Institute of Urban Environment, Chinese Academy of Sciences, Xiamen 361021, China*
[b] *CAS Center for Excellence in Regional Atmospheric Environment, and Key Laboratory of Urban Pollutant Conversion, Institute of Urban Environment, Chinese Academy of Sciences, Xiamen 361021, China*
[c] *Fujian Institute of Research on The Structure of Matter, Chinese Academy of Sciences, Fuzhou 350002, China*
[d] *Xiamen Institute of Rare-earth Materials, Haixi Institutes, Chinese Academy of Sciences, Xiamen 361021, China*
[e] *University of Chinese Academy of Sciences, Beijing 100049, China*

ABSTRACT

Infrared (IR) light serves as an attractive renewable source of solar energy for photothermal CO_2 methanation. Herein, we report the synthesis of Ni nanoparticles (NPs) supported on TiO_2 (Ni/TiO_2) derived from MIL-125(Ti) (MOFs), which achieves a CH_4 production rate of 271.9 mmol g_{Ni}^{-1} h^{-1} with nearly 100% selectivity and good durability at least 48 h under IR irradiation. The results indicate the catalytic performance is predominantly driven by thermal energy from efficient IR light conversion. IR light acts as the most effective light source and induces highest activity and CH_4 selectivity over $8Ni/TiO_2$ compared with UV–vis and full spectrum light. Highly-dispersed small-size Ni NPs, rich oxygen vacancies (OVs), strong adsorption capacity and enhanced CO_2 activation ability contribute to the high catalytic performance. OVs over Ni/TiO_2 play a crucial role in the CH_4 formation. This work demonstrates a feasible strategy towards the synthesis of MOF-derived catalysts for efficient photothermal CO_2 methanation.

1. Introduction

The massive consumption of unrenewable fossil fuels by human activities not only generates huge amounts of carbon dioxide (CO_2) to cause the greenhouse effect but also leads to energy shortages [1,2]. Consequently, researchers have invested increasing interest in developing different approaches to mitigate CO_2 effects, including the reduction of CO_2 emission at the source, CO_2 capture and sequestration and reutilization of CO_2 [3]. Ideally, converting CO_2 into value-added products or solar fuels such as CH_4 is supposed to be a two birds-one stone strategy, which can contribute to mitigating climate change and solving the problem of energy demand-supply deficit [4]. Commonly, it is efficient to CO_2 conversion using the thermal catalytic method, but it requires high temperature (150–500 °C) and pressure realized by vast energy consumption. Thus some alternative methods come into being, in which utilizing solar energy as a green source for CO_2 methanation is an important and attractive research domain [5]. A feasible method for

photocatalytic CO_2 reduction currently involves a positive photocatalyst which can photo-excite electrons to a high-energy state under ultraviolet (UV) and part of visible light irradiation [6]. However, on account of the wide band gap, poor light absorption, high charge carriers recombination and low ability to activate CO_2 molecules of traditional semiconductors, the utilization of the solar spectrum is limited and the efficiency of photocatalytic CO_2 conversion remains at a low level (in the range of $\mu mol\ g^{-1}\ h^{-1}$) far from the industrial application [7–9].

Recently, photothermal catalysis comes into sight as a promising approach to enhance the solar-to-fuel efficiency for CO_2 conversion due to its high catalytic efficiency and extended utilization of solar energy [10]. There are three interpretations of photothermal catalysis over the years: (1) solely solar energy serves to generate electron/hole pairs and heat, where photocatalysis and thermocatalysis are achieved severally. (2) Solar energy merely acts as the heating source to provide the photons, which can be transformed into thermal energy by the catalyst. Photo-driven thermal catalysis occurs when the surface temperature of

the catalyst reaches a certain value. The reaction under such circumstances still proceeds in the same way as the thermocatalytic process and photocatalysis plays minor role. (3) Solar energy coupling with thermal energy induces that photocatalysis and thermocatalysis take place synergistically [11,12]. Since the pioneering work of using Group VIII metals to photothermal catalytic CO_2 methanation by Ye and collaborators in 2014, great efforts have been made to exploit catalysts for photothermal CO_2 conversions [13]. It was investigated that the methanation performance at 190 ^{o}C over $Ru/TiO_{1.85}N_{0.15}$ catalyst could be immensely enhanced when visible light was introduced, and the turnover frequency of CO_2 was lifted to 15 from 7 h^{-1} [14]. The photothermal CO_2 methanation has been further improved on Ru/SiO_2 and Ru/SiNWs with the rates of 2.8 and 1 mmol g_{metal}^{-1} h^{-1}, respectively [15, 16]. Furthermore, over Cu_2O NPs supported on defective graphene, the CH_4 production rate of 14.93 mmol g_{Cu2O}^{-1} h^{-1} was achieved by coupling photo-thermal catalysis [17].

Up to now, the efficient reduction of CO_2 by solar energy remains an enormous challenge due to the shortage of high-efficiency catalysts and limitation of solar light absorbability especially in the infrared (IR) light region which accounts for ca. 53% of the solar energy arriving in the earth's surface [18,19]. Moreover, the IR wavelength is the main contributor of heat for photothermal CO_2 methanation catalysis [13,20]. However, converting CO_2 into carbon-based fuel by the IR light is still a tough assignment [21,22]. Therefore, the fabrication of the excellent IR-light absorbing materials is an emerging area of interest for improvement of photothermal CO_2 methanation. Transition metals always give admirable light-to-heat efficiency by the intra-/inter-band transitions, among which the abundant and low-cost Ni metal is an ideal candidate for CO_2 methanation [23]. However, the Ni catalysts tend to form metal carbonyl compounds during the CO_2 methanation process, resulting in the loss of intrinsic active phase and the passivation of active sites [24]. Employing an appropriate supporting material to enhance the surface chemistry and spatial confinement of Ni NPs gives a promising way to achieve sustainable CH_4 production from CO_2 [25]. Metal-organic frameworks (MOFs) possess inherited morphologies, large surface area, high-density immobilized metal sites, tunable size, and adjustable textural properties, which is attractive to function as the precursor for preparing Ni composite catalysts and endows great potential for CO_2 reduction [26–28]. Composites derived from suitable MOFs precursors are provided with steady structural and chemical stabilities, prospective morphologies and enhanced interfacial interactions under controlled pyrolysis conditions, and meanwhile they can enable supported components to distribute homogeneously with scarcely agglomerations [29,30]. The previous study shows that $Ga-Cu/CeO_2$ with highly-dispersed Ga and Cu species synthesized from Ce-based MOFs exhibits the superior CO production rate in photothermal CO_2 hydrogenation [31].

With these motivations, we designed a series of xNi/TiO_2 catalysts by employing a Ti-based MOF (MIL-125(Ti)) as the template to support Ni nanoparticles (NPs). Dynamic photothermal catalytic CO_2 hydrogenation reaction over these catalysts under IR irradiation was carried out. The $8Ni/TiO_2$ displays nearly 100% selectivity towards CH_4 and a remarkable production rate of 271.9 mmol g_{Ni}^{-1} h^{-1}. Meanwhile, the catalytic stability on $8Ni/TiO_2$ can maintain at least 48 h, exhibiting considerably superior catalytic performance in comparison to 8Ni/P25. The controlled experiments manifest that IR is the optimal light source to achieve the high activity and selectivity over $8Ni/TiO_2$ for photothermal CO_2 methanation, while UV–vis or full spectrum light leads to low yield and selectivity of CH_4. The physicochemical characteristics of $8Ni/TiO_2$ demonstrate that high-dispersion of small-size Ni NPs, enhanced light absorption and light-to-heat conversion ability, sufficient surface oxygen vacancies and strong gas adsorption capacity are responsible for the outstanding catalytic performance of CO_2 methanation. The investigation of in situ infrared spectra reveals that the different reaction pathways for the formation of CH_4 and CO are impacted by oxygen vacancies. This study clearly offers an anticipant

Table 1
Element composition and properties of samples.

Catalysts	Ni loading (wt%)	S_{BET} (m^2/g)	D_{BJH} (nm)	Total pore volume (cm^3/g)	Ni NPs size (nm)[a]	Ni NPs size (nm)[b]
TiO_2	0	84.0	13.9	0.21	–	–
$5Ni/TiO_2$	5.1	146.3	9.7	0.36	9.1	8.1
$8Ni/TiO_2$	8.0	131.6	9.3	0.31	10.6	10.0
$10Ni/TiO_2$	10.1	60.7	13.7	0.25	11.5	10.5
8Ni/P25	7.9	82.7	15.3	0.32	17.7	20.0

[a] Calculated by Scherrer equation based on the Ni (111) diffraction peak determined by XRD.
[b] Determined by TEM images.

strategy for manufacturing Ni-based composite catalysts by MOF-derived method to achieve high efficiency of photothermal CO_2 methanation.

## 2. Experimental section

2.1. Chemicals and materials

All the used reagents and solvents of analytical grade were obtained without further purification. Commercial P25, titanium tetraisopropanolate ($C_{12}H_{28}O_4Ti$), nickel nitrate hexahydrate ($Ni(NO_3)_2 \cdot 6HH_2O$), terephthalic acid (H_2BDC, $C_8H_6O_4$), methanol (CH_3OH), and N, N-dimethylformamide (DMF, C_3H_7NO) were purchased from Sinopharm Chemical Reagent Co., Ltd.

2.2. Preparation of catalysts

MIL-125(Ti) was prepared by a reported solvothermal method with a slight modification [32]. Typically, 6 mL of methanol and 54 mL of DMF were added to a conical flask and stirred evenly. 3.53 g of terephthalic acid was dissolved in the as-obtained solution and stirred for 30 min, and then 2.1 mL of isopropyl titanate as titanium source was added and stirred for another 30 min. Next, the uniformly mixed solution was sealed in a 100 mL Teflon-lined stainless-steel autoclave and put in an oven at 150 °C for 16 h. After the autoclave was cooled down, the sample was centrifuged out and then immersed into methanol for 12 h to remove excess DMF, finally dried under vacuum at 80 °C overnight.

The xNi/TiO_2 catalysts were prepared by the wet impregnation method. Firstly, 1 g of MIL-125(Ti) was dispersed into 100 mL of deionized water and ultrasonicated at room temperature for 10 min. Then, a quantitative $Ni(NO_3)_2 \cdot 6 H_2O$ solution was added and the resulting solution was stirred at room temperature for 6 h. After being filtered and washed with deionized water for three times, the product was collected and dried at 80 °C overnight. Then the aqua solids were obtained and calcined in the air (100 mL/min) at 450 °C for 6 h, followed by a thermal reduction process at 400 ^{o}C for 3 h under a flow of H_2 (30 mL/min). The as-obtained samples were denoted as xNi/TiO_2 (x = 5, 8 and 10) and the weight percentage (x) of Ni content in xNi/TiO_2 was determined by an inductively coupled plasma optical emission spectrometer (ICP-OES) to be 5.1%, 8.0% and 10.1% (Table 1), respectively.

As a comparison, the reference compound 8Ni/P25 was prepared by utilizing P25 as the support to replace MIL-125(Ti). The dry impregnation method was used to give the similar Ni content to $8Ni/TiO_2$. Typically, 100 mg of P25 was dispersed into 100 mL of deionized water and ultrasonicated at room temperature for 10 min. Then, a quantitative $Ni(NO_3)_2 \cdot 6 H_2O$ solution was added and the resulting solution was stirred at 80 ^{o}C until dry. The obtained solid sample followed the same calcination and hydrogen condition as $8Ni/TiO_2$. Ni content of 8Ni/P25 was analyzed by ICP-OES to be 7.9% (Table 1). Pure TiO_2 in this work
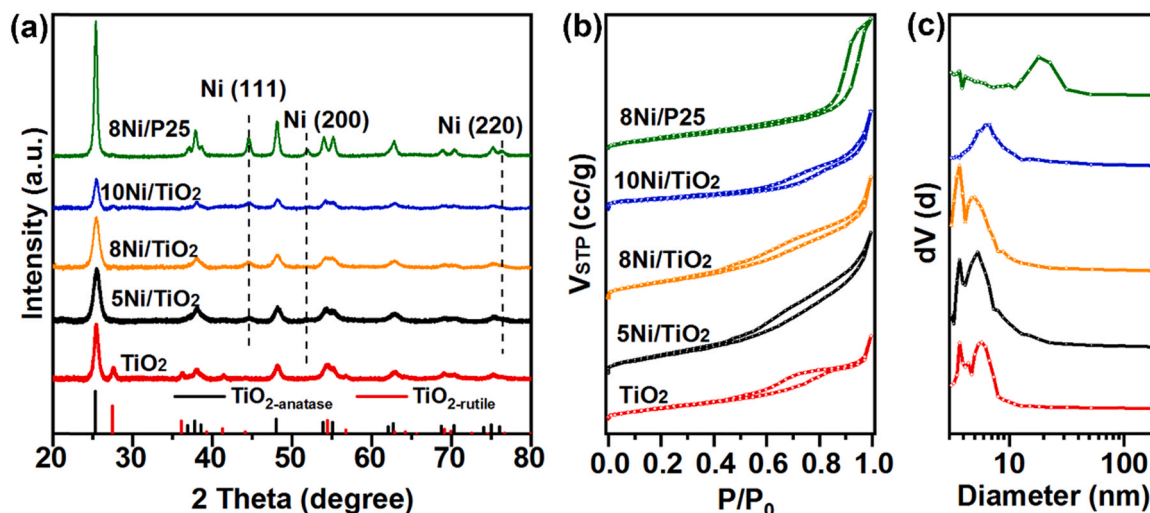
Fig. 1. (a) XRD patterns, $TiO_{2\text{-antase}}$ and $TiO_{2\text{-rutile}}$ represents JCPDS PDF # 01–071–1166, JCPDS PDF # 01-086-0147, respectively; (b) N_2 adsorption-desorption isotherms; (c) Pore distribution of samples.

was synthesized by directly calcining MIL-125(Ti) at 450 °C for 6 h in air (100 mL/min) and then reduced by H_2 (30 mL/min) at 400 °C for 3 h.

2.3. Characterization

The Ni content in samples were analyzed by ICP-OES. The crystalline nature of all samples was measured by X-ray diffraction (XRD) characterization on an X'Pert Pro automatic powder diffractometer using Cu Kα monochromatized radiation (40 kV, 40 mA). Transmission electron micrography (TEM) and high-resolution TEM (HRTEM) images were taken from a JEM 2100 F electronic microscopy operated at 200 kV. Elemental distribution of samples was detected by using energy-dispersive spectroscopy (EDS), equipped on the TEM. Nitrogen adsorption-desorption measurements were performed on a Quantachrome Autosorb IQ instrument to measure the average diameter (D_{BJH}) and specific surface area (S_{BET}) of the sample, using the Barrett-Joyner-Halenda (BJH) and Brunauer-Emmett-Teller (BET) methods, respectively. The chemical states of catalysts were examined by a Kratos/Shimadzu X-ray photoelectron spectroscopy (XPS, AXIS Supra) with Al-Kα radiation (1486.6 eV). A Varian Cary 5000 ultraviolet-visible spectrophotometer was used to record the diffuse reflectance spectrum (DRS) in the range of 200–2500 nm at room temperature with $BaSO_4$ as a reference. The low temperature electron paramagnetic resonance (EPR) spectroscopy was carried out on an A300 spectrometer at the liquid nitrogen temperature, where 10 mg of powder was weighed and put into the sample tube for testing. The hydrogen temperature-programmed reduction (H_2-TPR), CO_2 temperature-programmed desorption (CO_2-TPD), H_2 temperature-programmed desorption (H_2-TPD), and CO pulse adsorption tests were performed on a ChemStar TPx chemisorption analyzer with a TCD detector of Quantachrome Company. The detailed process of H_2-TPD: Firstly, 50 mg of sample was reduced in $5\%H_2$/Ar mixture (30 mL/min) at 400 °C for 1 h and then the gas was switched to Ar flow (30 mL/min) at the same temperature for 1 h. Subsequently, the sample was cooled down to 30 °C and $5\%H_2$/Ar flow (absorption gas, 30 mL/min) was introduced again for 1 h to be fully absorbed on the sample, and then purged with Ar (30 mL/min for 0.5 h) to remove physically adsorbed hydrogen. Finally, H_2-TPD was performed by heating the sample from 30 °C to 450 °C with a heating rate of 10 °C/min in Ar. The desorbed hydrogen was detected by the TCD detector. CO_2-TPD was carried out using a similar procedure (in situ reduced in $5\%H_2$/Ar atmosphere at 400 °C firstly, then cooling slowly by He gas flow), except that CO_2 was used as the adsorption gas.

In the case of H_2-TPR measurements, 50 mg of sample was kept

under constant $5\%H_2$/Ar flow (30 mL/min), and the temperature was increased from 25 °C to 750 °C with a heating ramp of 10 °C/min. During the CO pulse adsorption experiment, the samples were firstly pretreated by $5\%H_2$/Ar (30 mL/min) gas at 400 °C as well and then cooled down to 50 °C in the Ar atmosphere. The CO pulse process was performed at 50 °C using $5\%CO$/He. *In situ* DRIFTS was operated on a FTIR spectrometer (Nicolet Nexus 670) equipped with a smart collector and a MCT detector. Prior to experiment, the sample was pretreated in a $5\%H_2$/Ar gas flow for 1 h at 400 °C, then cooled down to room temperature by He flow. Subsequently, the mixed reaction gas (10 vol% CO_2, 40 vol% H_2, and 50 vol% He) at a flow rate of 10 mL/min was filled into the cell and followed by heating to the certain temperature with a ramping rate of 10 °C/min.

2.4. Catalytic activity evaluation

Photothermal CO_2 hydrogenation tests were evaluated in a cylindrical stainless- steel reactor with a quartz window. An IR lamp (375 W, Philips) was employed as the IR light source. A xenon lamp (PLS-SXE300UV, Beijing PerfectLight Technology Co. Ltd.) was used as the full spectrum light and UV–vis light (using an optical filter) source. For all experiments, 40 mg of catalyst was firstly dispersed into an ethanol suspension and coated on a fiberglass membrane of 50 mm diameter, dried at 70 °C, and finally placed on the reactor. A thermocouple was located at the center of the catalyst surface to monitor the surface equilibrium temperature (T_{eq}) of the catalyst bed under irradiation. Next, a continuous flow of the gas mixture (the volume ratio of CO_2/H_2/He = 1/4/5) was introduced into the stainless-steel reactor at a rate of 10 mL/min. An online GC equipped with an FID and TCD detector was employed to determine the concentrations of CO_2, CO and CH_4.

Thermal catalytic activity was inspected in a tube-type resistance furnace. Specifically, 40 mg of the catalyst and 1 g of silica sand (sized as 40–60 mesh) were mixed in a silica tube and placed into the furnace. Then the feed gas of 10 vol% CO_2, 40 vol% H_2, and 50 vol% He (10 mL/min) was passed through the sample with a heating rate of 10 °C/min. The photocatalytic activity of the catalyst for CO_2 reduction was measured at low temperature by using an ice-water bath.

The production rate of CH_4 (r_{CH4}) and CO (r_{CO}) conversions were calculated respectively according to the following Eqs. (1) and (2):

$$r_{CH_4} = \frac{n_{CH_4}}{\text{Weight of catalyst} \times W_{Ni}} \times 60 \quad (\text{mmol} \quad g_{Ni}^{-1}h^{-1}) \qquad (1)$$
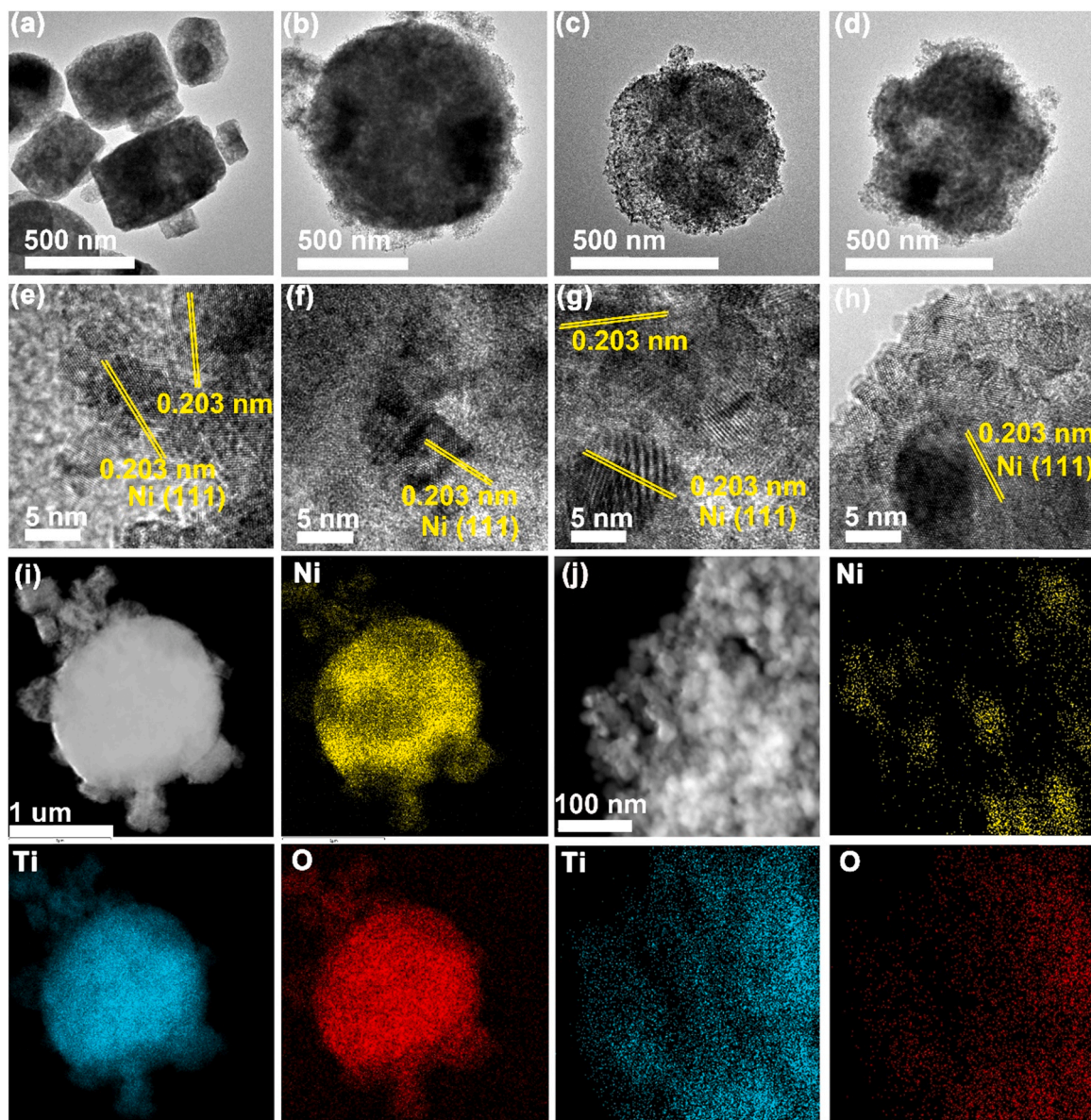
Fig. 2. TEM images: (a) TiO$_2$, (b) 5Ni/TiO$_2$, (c) 8Ni/TiO$_2$, (d) 10Ni/TiO$_2$; HRTEM images: (e) 5Ni/TiO$_2$, (f) 8Ni/TiO$_2$, (g) 10 Ni/TiO$_2$, (h) 8Ni/P25; Element mapping images: (i, j) 8Ni/TiO$_2$ and 8Ni/P25.

$$r_{CO} = \frac{n_{CO}}{\text{Weight of catalyst} \times W_{Ni}} \times 60 (\text{mmol} \quad g_{Ni}^{-1}h^{-1}) \qquad (2)$$

where,

$$n_{CH4} = \frac{F \times [CH_4]}{22.4}$$

$$n_{CO} = \frac{F \times [CO]}{22.4}$$

The selectivity of CH$_4$ and CO was estimated by the Eqs. (3) and (4):

$$\text{The selectivity of CH}_4 \ (\%) = \frac{[CH_4]}{[CH_4] + [CO]} \times 100\% \qquad (3)$$

$$\text{The selectivity of CO} \ (\%) = \frac{[CO]}{[CH_4] + [CO]} \times 100\% \qquad (4)$$

Here, W_{Ni} denotes the nickel-metal loading (wt%), and F represents the gas flow rate (mL min^{-1}), noting that Eqs. (1) and (2) are multiplied by 60 because the yield is calculated by per hour; [CH$_4$] and [CO] are the respective concentration (vol%) of CH$_4$ and CO detected by online GC.

3. Results and discussion

3.1. Structural and morphological characterizations

XRD patterns of all samples are shown in Fig. 1a. Pure TiO$_2$ derived from MIL-125(Ti) clearly shows the characteristic peaks of two crystal phases of anatase (JCPDS PDF # 01–071–1166) and rutile (JCPDS PDF # 01-086-0147) on the XRD pattern. The introduction of Ni species in TiO$_2$ results in the disappearance of rutile phase. As observed for the XRD patterns of xNi/TiO$_2$ (x = 5, 8, 10), only peaks attributed to anatase phase are present that are obviously widened and weakened with the increasing of Ni content. It indicates that the existence of Ni species and its content can largely influence the crystallization process of TiO$_2$ during the pyrolysis of MIL-125(Ti) due to the inhomogeneity of the stress and the lattice parameter by strong interaction between TiO$_2$ and Ni NPs [4]. The XRD pattern of the reference sample 8Ni/P25 only exhibits the stronger peaks of anatase phase and also the typical
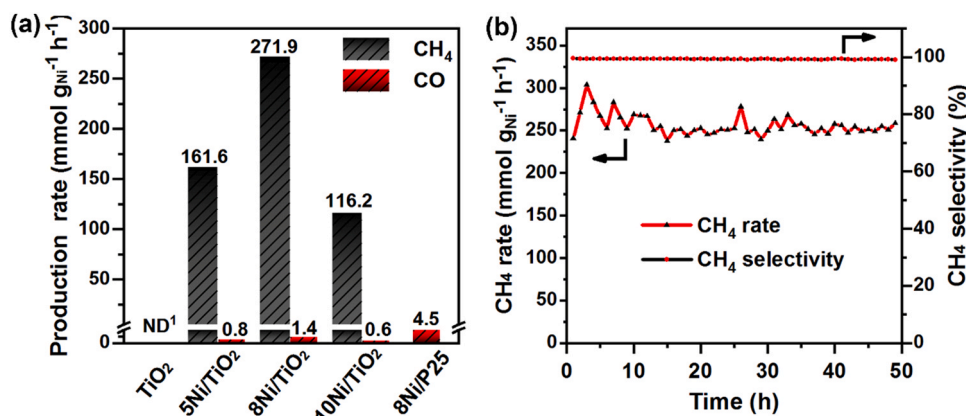
Fig. 3. Production rate in the initial 3 h (a) and durability test (b); [1]No detected; Reaction condition: the samples were under IR light irradiation (1230 mW/cm^2) with a continuous flow of 10 vol% CO_2, 40 vol% H_2 and 50 vol% He at a rate of 10 mL/min.

characteristic peaks of metallic Ni (JCPDS PDF # 96–210–2270) at the 2θ of around 44.5°, 51.8° and 76.4° indexed to the (111), (200) and (220), respectively. However, it is inconspicuous to the peaks of metallic Ni in all xNi/TiO$_2$, where only a small and faint peak at 44.5° for Ni (111) plane can be observed. It manifests that metallic Ni NPs existed in xNi/TiO$_2$ are small-size and high-dispersed state [33]. The size of Ni NPs in xNi/TiO$_2$ is calculated by Scherrer equation based on the Ni (111) diffraction peak and is approximately in the range of 9.1–11.5 nm (Table 1), which is much smaller than that of 8Ni/P25 (the NPs size of Ni is around 17.7 nm). It also reveals that the formed strong interaction of Ni species and TiO$_2$ in the conversion process of catalyst endows Ni NPs with the better resistance of sintering and maintains small size of Ni NPs. Generally, the high-dispersion and small-size Ni NPs are the key to high activity for CO_2 methanation [34].

Nitrogen static adsorption−desorption isotherms are depicted in Fig. 1**b**. Pure TiO$_2$ exhibits typical features of type IV isotherms with H4 hysteresis loops, while all xNi/TiO$_2$ belong to type IV isotherms with H3 hysteresis loops that indicate the presence of the more irregular mesoporous structure [35]. The breadth of the hysteresis loops is influenced by the content of Ni NPs and become narrower with more Ni NPs loading. The pore size distribution curves calculated by Barrett–Joyner–Halenda (BJH) methods are provided in Fig. 1**c**. The S$_{BET}$, pore volume, and pore size of samples are summarized in Table 1. The structural parameters of xNi/TiO$_2$ are closely related to the loading content of Ni in the samples. The S$_{BET}$ of pure TiO$_2$ is 84.0 m^2/g, while 5% Ni content was introduced, it is dramatically enhanced to as high as 146.3 m^2/g. However, with the loading of 8% Ni or even more, the value of S$_{BET}$ starts to decrease, as observed for 8Ni/TiO$_2$ of 131.6 m^2/g and 10Ni/TiO$_2$ of 60.7 m^2/g. Evidently, 10Ni/TiO$_2$ exhibits a much lower S$_{BET}$ than that of pure TiO$_2$. The similar trend is also reflected in the variation of pore volume for xNi/TiO$_2$. It can be reasonably explained that a small amount of Ni species in the matrix of MIL-125(Ti) precursor sustains the intrinsic structure to avoid excessive shrinkage in the pyrolysis process [36]. Nevertheless, when excess Ni species enters into the pore of MIL-125(Ti) precursor, it facilitates the formation of the very strong interaction between the Ni and Ti species and further observes the existence of NiTiO$_3$ in the unreduced 10Ni/TiO$_2$ (Fig. S1), It accelerates the decomposition of organic ligand and the shrinkage of structure to finally decrease the pore volume and S$_{BET}$ of 10Ni/TiO$_2$. These results suggest that the introduction of moderate content of Ni species is conducive to preserving the original structure of the MOF template partly and generating larger S$_{BET}$ and pore volume. As a comparison, 8Ni/P25 only owns the lower S$_{BET}$ of 82.7 m^2/g than 8Ni/TiO$_2$, though they have the almost same pore volume.

Fig. 2**a-d** displays the representative TEM images of samples. It can be seen that pure TiO$_2$ shows regular tablet-like morphology with a size range of 300–500 nm. Catalysts 5Ni/TiO$_2$ and 8Ni/TiO$_2$ keep the similar morphology as pure TiO$_2$ but exhibit more mesoporous and looser structure to provide sufficient channels for gas adsorption [19]. Whereas, the morphology of 10Ni/TiO$_2$ becomes more irregular and broken. It demonstrates that a moderate amount of Ni loading is in favor of maintaining the morphology. TEM image of the comparative sample 8Ni/P25 shown in Fig. S2 presents irregular morphology with size of ~20 nm. HRTEM images are displayed in Fig. 2**e-h**. For Ni-containing samples, the spacing of lattice fringes are clearly measured to be 0.203 nm that are ascribed to the lattice plane (111) of metallic Ni. The size of Ni NPs estimated from HRTEM images is listed in Table 1 to be 8.1, 10.0, 10.5 and 20.0 nm for 5Ni/TiO$_2$, 8Ni/TiO$_2$, 10Ni/TiO$_2$ and 8Ni/P25, respectively, which is well in consistent with the calculated results based on XRD characterization. The element mapping images of 8Ni/TiO$_2$, as depicted in Fig. 2**i**, obviously indicate all elements (Ti, O and Ni) are uniform distribution on sample compared to 8Ni/P25 (Fig. 2**j**). CO pulse chemisorption has been performed to further investigate the Ni dispersion (Table S1), in which the Ni dispersion of 8Ni/TiO$_2$ (8.9%) is far beyond that of 8Ni/P25 (1.3%). The highly-dispersed NPs are commonly thought to provide more active sites to participate in the catalytic process [35]. These results demonstrate that 8Ni/TiO$_2$ obtained derived from MOFs pyrolysis can effectively generate higher-dispersed smaller-size Ni NPs than 8Ni/P25, providing full prerequisites for the catalytic of CO_2 methanation.

3.2. Photothermal catalytic performance for CO_2 reduction

IR light-driven photothermal catalytic CO_2 reduction by H_2 over the synthesized catalysts was performed in a stainless-steel reactor with a quartz window. A feed stream of 10 vol% CO_2, 40 vol% H_2 and 50 vol% He constantly flows into the reactor with a rate of 10 mL/min. As displayed in Fig. 3**a**, no products can be detected over pristine TiO$_2$, indicating that neither photocatalytic nor photothermal catalytic activity occurs under this condition. However, for xNi/TiO$_2$, the obvious catalytic activity can be observed with the products of CH$_4$ and CO. The production rates of CH$_4$ (r_{CH_4}) and CO (r_{CO}) for 5Ni/TiO$_2$ are found to be 161.6 mmol g$_{Ni}^{-1}$ h^{-1} and 0.8 mmol g$_{Ni}^{-1}$ h^{-1}, respectively, which can be further increased to 271.9 mmol g$_{Ni}^{-1}$ h^{-1} and 1.4 mmol g$_{Ni}^{-1}$ h^{-1} over 8Ni/TiO$_2$. When Ni content is further increased to 10%, the catalytic activity of 10Ni/TiO$_2$ reduces to 116.2 mmol g$_{Ni}^{-1}$ h^{-1} of r_{CH_4} and 0.6 mmol g$_{Ni}^{-1}$ h^{-1} of r_{CO}. Besides, the control experiment using 10%H_2/Ar to replace CO_2/H_2/He as reaction gas was conducted and no products were detected (Fig. S3a). Therefore, it can deduce that CH$_4$ and CO on xNi/TiO$_2$ are produced from the feed gas (CO_2/H_2/He) rather than adventitious carbon contaminants. All xNi/TiO$_2$ catalysts exhibit the high reaction rates with nearly 100% selectivity of CH$_4$, among which 8Ni/TiO$_2$ possesses the highest production rate of CH$_4$. As a comparison, the photothermal performance of 8Ni/P25 is glaringly different in the
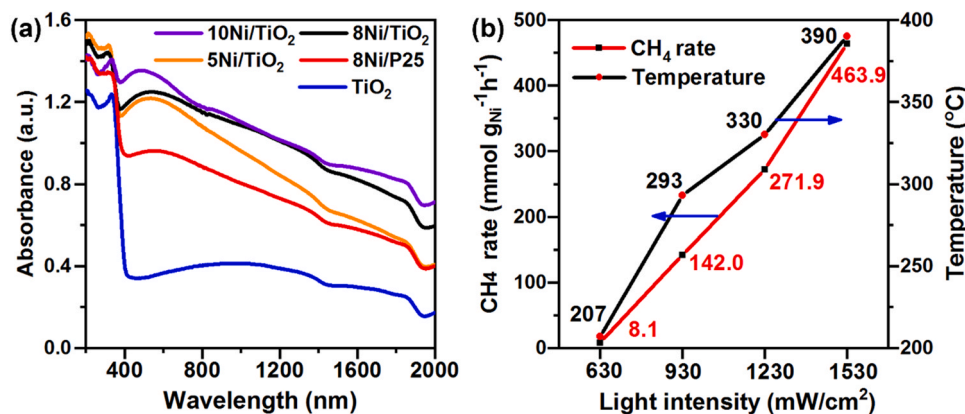
Fig. 4. (a) DRS spectra of samples, (b) CH_4 formation rate and equilibrium temperature of $8Ni/TiO_2$ under different intensity of IR light.

activity and selectivity with $8Ni/TiO_2$. It only shows a low production rate of CO as 4.5 mmol g_{Ni}^{-1} h^{-1} and no CH_4 is observed. Additionally, CO_2 reduction on pure P25 has been investigated under the same reaction conditions and shows no activity (Fig. S3b).

Taking into account the rapid deactivation due to thermodynamically inevitable carbon deposition during the reaction process [37], the catalytic durability test of CO_2 hydrogenation was performed under IR light irradiation for 48 h, as illustrated in Fig. 3b. The CH_4 production rate increases slightly within 3 h mainly because of the reduction of surface NiO species to metallic Ni, and then maintains at an impressive value of ~ 250 mmol g_{Ni}^{-1} h^{-1}. In addition, CH_4 selectivity is observed to be stable and remains over 99%. The XRD pattern (Fig. S4), TEM and HRTEM images (Figs. S5a and 5b) of the used $8Ni/TiO_2$ display no obvious change compared to the fresh catalyst, also confirming the structure stability of $8Ni/TiO_2$ during the reaction. It can be inferred that the deactivation phenomenon during the CO_2 reduction process can be mitigated on $8Ni/TiO_2$. Moreover, the recently reported CO_2 hydrogenation based on photothermal catalysis is summarized in Table S2. Apparently, $8Ni/TiO_2$ in this work exhibits the considerable catalytic performance. Therefore, The Ni supported on TiO_2 derived from MIL-125(Ti) is confirmed to be a preferential catalyst of high activity, selectivity and stability for photothermal CO_2 methanation.

3.3. Relationship between light and photothermal catalytic performance

To unveil the role of IR light in the photothermal catalytic performance, the optical response of the catalysts was evaluated by DRS measurement, as displayed in Fig. 4a. Pure TiO_2 shows a typical intense

Table 2
Catalytic performance of $8Ni/TiO_2$ under different light irradiation.

Treatment	Light intensity (mW/cm²) and T_{eq} (°C)	Production rate (mmol g_{Ni}^{-1} h^{-1})		Selectivity (%)	
		CO	CH_4	CO	CH_4
IR[a]	630, 207	0.04	8.1	0.4	99.6
IR[a]	1230, 330	1.4	271.9	0.5	99.5
UV–vis-IR[b]	1230, 198	2.4	6.3	27.7	72.3
UV–vis-IR[b]	1230, 114[c]	0	0	0	0
UV–vis[b]	800, 160	0.02	0.04	30.3	69.7
UV–vis[b]	800, 69[c]	0	0	0	0

[a] Infrared light was conducted by using light source of IR lamp (375 W, Philips).
[b] Irradiation was conducted by using light source of PLS-SXE300UV (Perfect Light).
[c] Surface temperature of the catalyst layer was controlled by an ice−water bath.

absorption of UV region but possesses the poor absorption under visible and IR regions. In contrast, all xNi/TiO_2 show extraordinarily high absorption across the whole solar spectrum. The significantly enhanced absorption in the Vis-IR region can be ascribed to the localized surface plasmon resonance of the Ni NPs [38]. The light absorption ability of the catalysts over the measured illumination range can be ordered as follows: TiO_2 < $8Ni/P25$ < $5Ni/TiO_2$ < $8Ni/TiO_2$ < $10Ni/TiO_2$. Notably, xNi/TiO_2 displays a much stronger intensity of absorbance in the whole region than $8Ni/P25$. It is mainly due to that the porous channel structure of TiO_2 support allows light to be multiply reflected in the interior cavity [39]. We also monitor the surface temperature of the catalysts to study the function of IR light during the reaction process (Fig. S6a). The results can be sorted as: TiO_2 (223 °C) < $5Ni/TiO_2$ (315 °C) < $8Ni/P25$ (319 °C) < $8Ni/TiO_2$ (330 °C) < $10Ni/TiO_2$ (338 °C), which is basically consistent with the order of light absorption ability. In particular, $5Ni/TiO_2$ possesses the stronger absorption of IR light but displays slightly lower reaction temperature than $8Ni/P25$. It can be reasonably attributed to the lower loading of Ni NPs that are the sites for light-to-heat conversion. The surface temperature of xNi/TiO_2 is much higher than that of pure TiO_2 and is closely relevant to the Ni content, verifying strong ability of light-to-heat with the introduction of Ni species. Therefore, xNi/TiO_2 prepared by MOFs template can be expected to be an efficient IR-light photo absorber which owns the excellent photo-thermal conversion. Generally, photothermal catalyst is thought to raise the surface temperature by light-to-heat effect and then provide enough thermal energy to promote or drive the catalysis [12]. To assess which of the pathways was predominant in the system, we firstly carried out the control experiment over $8Ni/TiO_2$ by utilizing external electric heating in a resistance furnace to replace IR irradiation. As shown in Fig. S6b, the discrepancy of the production rates obtained by IR irradiation (r_{CH4} = 271.9 mmol g_{Ni}^{-1} h^{-1}, r_{CO} = 1.4 mmol g_{Ni}^{-1} h^{-1}) and electric heating (r_{CH4} = 275.0 mmol g_{Ni}^{-1} h^{-1}, r_{CO} = 1.4 mmol g_{Ni}^{-1} h^{-1}) can be negligible at the same surface temperature of 330 °C. Furthermore, we also explored the experiment on $8Ni/TiO_2$ by varying the intensity of IR light. As shown in Fig. 4b, under IR light intensities of 630, 930, 1230 mW/cm², the corresponding CH_4 production rates and surface temperatures of $8Ni/TiO_2$ are 8.1, 142.0, 271.9 mmol g_{Ni}^{-1} h^{-1} and 207, 293, 330 °C, respectively. Meanwhile, all of them show the selectivity for CH_4 near 100%, as depicted in Fig. S7. When the light intensity is fortified to 1530 mW/cm², the surface temperature of $8Ni/TiO_2$ arrives at 390 °C, where the catalyst still shows the high CH_4 selectivity over 98% and displays a maximum r_{CH4} of 463.9 mmol g_{Ni}^{-1} h^{-1}. Moreover, $8Ni/TiO_2$ exhibits theoretical carbon balance equal to 100% (Fig. S7) under different light intensity, further indicating that there are no other products produced during the reaction. The results show a nearly positive linear relationship between the production rate and light intensity. The surface temperature of the catalyst is controlled by the intensity of the light, which is a decisive factor to affect catalytic activity of
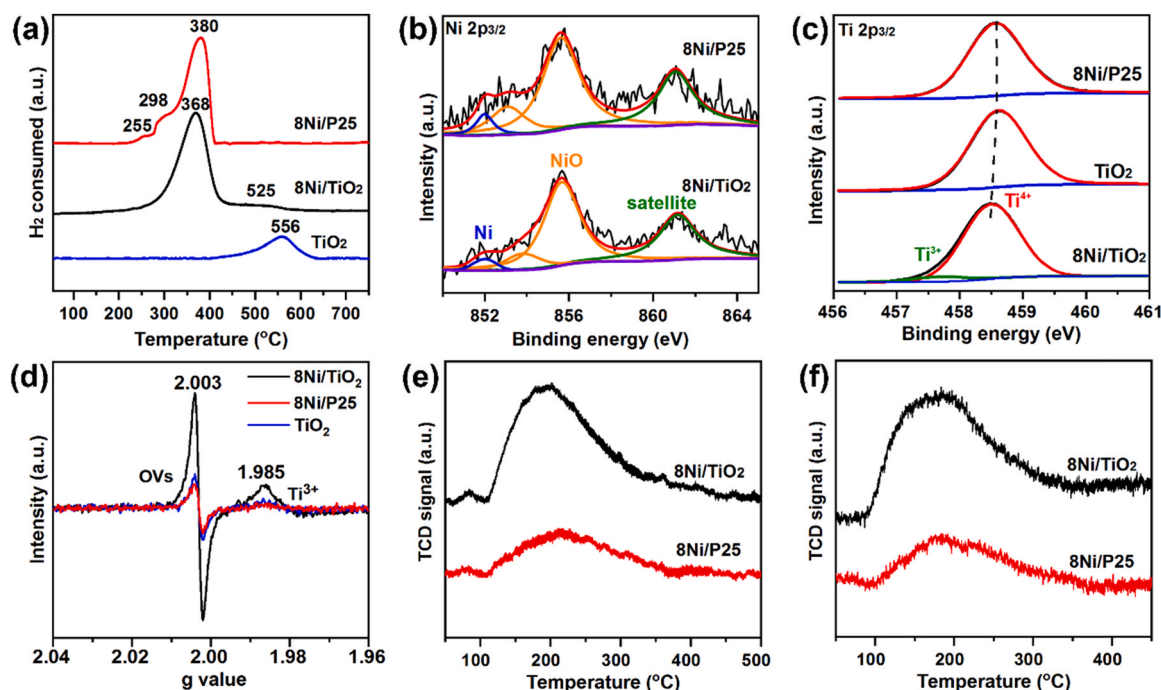
Fig. 5. (a) H_2-TPR profiles of 8NiO/P25 (the precursor of 8Ni/P25), 8NiO/TiO_2 (the precursor of 8Ni/TiO_2), unreduced TiO_2; (b-c) XPS spectra of Ni 2p3/2 and Ti 2p3/2; (d) EPR spectra; (e-f) CO_2-TPD and H_2-TPD profiles.

8Ni/TiO_2. This is a strong evidence that IR light promoting CO_2 methanation over 8Ni/TiO_2 should be closely related to a photo-driven thermal catalysis [40]. The photocatalytic activity of 8Ni/TiO_2 for CO_2 reduction was carried out with an ice-water bath under IR irradiation of 1230 mW/cm^2, as displayed in Fig. S8. In this case, neither distinct photo-reduction of CO_2 nor the discernable generation of CH_4 or CO can be observed when the surface temperature of 8Ni/TiO_2 reduces to 98 °C. This indicates that 8Ni/TiO_2 is photocatalytically inert toward CO_2 reduction under IR light at low temperature. Therefore, it can be summed up that IR light in this system functions as a heating source to stimulate CO_2 methanation over 8Ni/TiO_2. In addition, although 8Ni/P25 has the similar equilibrium reaction temperature to xNi/TiO_2, it displays much lower catalytic activity and different product. Thus, we can infer the temperature is not an absolute influence factor responding to the distinction of the catalytic performance for 8Ni/P25 and xNi/TiO_2.

To further investigate how light region affects the catalytic reduction of CO_2, the catalytic performance of 8Ni/TiO_2 has been evaluated under controlled conditions. As listed in Table 2, the obtained r_{CH4} (6.3 mmol g_{Ni}^{-1} h^{-1}) and T_{eq} (198 °C) under irradiation of UV–vis-IR light (1230 mW/cm^2) are much lower than r_{CH4} (271.9 mmol g_{Ni}^{-1} h^{-1}) and T_{eq} (330 °C) under the same IR light intensity (1230 mW/cm^2). When with the similar equilibrium temperature, r_{CH4} under UV–vis-IR light (198 °C, 6.3 mmol g_{Ni}^{-1} h^{-1}, 1230 mW/cm^2) is close to that under IR irradiation (207 °C, 8.1 mmol g_{Ni}^{-1} h^{-1}, 630 mW/cm^2). These manifest that the thermal energy from light-to-heat conversion is crucial to the formation of CH_4. However, r_{CO} (2.4 mmol g_{Ni}^{-1} h^{-1}) becomes higher under UV–vis-IR light with CH_4 selectivity reduced to 72.3%. By using the optical filter to cut off the IR region, lowest r_{CH4} (0.04 mmol g_{Ni}^{-1} h^{-1}) and CH_4 selectivity (69.7%) are observed under UV–vis irradiation light of 800 mW/cm^2 at 160 °C. The results verify that the existence of UV–vis promotes the production of CO and plays little role to the formation of CH_4. When the surface layer of 8Ni/TiO_2 is controlled at low temperature, neither CO nor CH_4 is detected under the UV–vis or full light spectrum, demonstrating no photocatalysis occurs over the catalyst. Hence, IR light serves as the most efficient light source for photothermal CO_2 methanation over 8Ni/TiO_2.

3.4. The origin of enhanced photothermal catalytic performance

To further figure out the reason why 8Ni/TiO_2 and 8Ni/P25 displayed glaringly obvious difference in the activity and selectivity, H_2-TPR was firstly performed to investigate the reducibility of unreduced samples and the interaction between Ni species and support, as shown in Fig. 5a. 8NiO/P25 (the precursor of 8Ni/P25 catalyst) displays three main peaks of H_2 consumption at 255, 298 and 380 °C, which can be assigned to the reduction of different NiO existed by weak or strong interaction with P25 [41]. The only main peak centered at 368 °C is observed for 8NiO/TiO_2 (the precursor of 8Ni/TiO_2 catalyst), revealing that well-dispersed NiO species by significant interaction with TiO_2 becomes dominant [42]. Notably, an additional wide shoulder peak in 400–560 °C is observed. It possibly belongs to the reduction of strongly interacted NiO on TiO_2 and a partial reduction of Ti^{4+} to Ti^{3+}. Moreover, the reduction temperature of Ti^{4+} over 8NiO/TiO_2 is much lower than that of unreduced pure TiO_2 (556 °C). It also confirms the strong interaction between NiO and TiO_2 in 8NiO/TiO_2, which may consequently ameliorate the redox capacity of TiO_2 and lead to the formation of surface defects [43]. XPS spectra reveal the surface electronic state of elements as shown in Figs. 5b and 5c. The Ni 2p3/2 spectra of 8Ni/TiO_2 and 8Ni/P25 show the peaks at the binding energies of 852.0 eV attributing to metallic Ni species and the shake-up satellite peak at 861.1 eV. The characteristic peaks of Ni^{2+} can be observed since the surface of reduced samples is partially oxidized in air during the transfer process of sample to XPS instrument. The peaks of Ni^{2+} located at 853.1 and 855.6 for 8Ni/P25 are observed to shift slightly to a higher value of 853.9 and 855.7 eV for 8Ni/TiO_2. It further suggests the stronger interaction between Ni NPs and TiO_2 support on 8Ni/TiO_2 [44]. Due to the presence of the rutile phase, the binding energy of characteristic Ti^{4+} 2p3/2 peak at 458.6 eV in TiO_2 and 8Ni/P25 is slightly higher than that of 8Ni/TiO_2 (Fig. 5c) [45,46]. Interestingly, 8Ni/TiO_2 also shows another peak at 457.7 eV assigned to Ti^{3+} 2p3/2, revealing more surface defects exited in 8Ni/TiO_2 [47]. To investigate the defects of catalysts, the low temperature EPR was carried out and displayed in Fig. 5d. A weak peak assigned to the presence of OVs is observed at g = 2.003 for 8Ni/P25 and TiO_2. In contrast, 8Ni/TiO_2 shows a much stronger signal
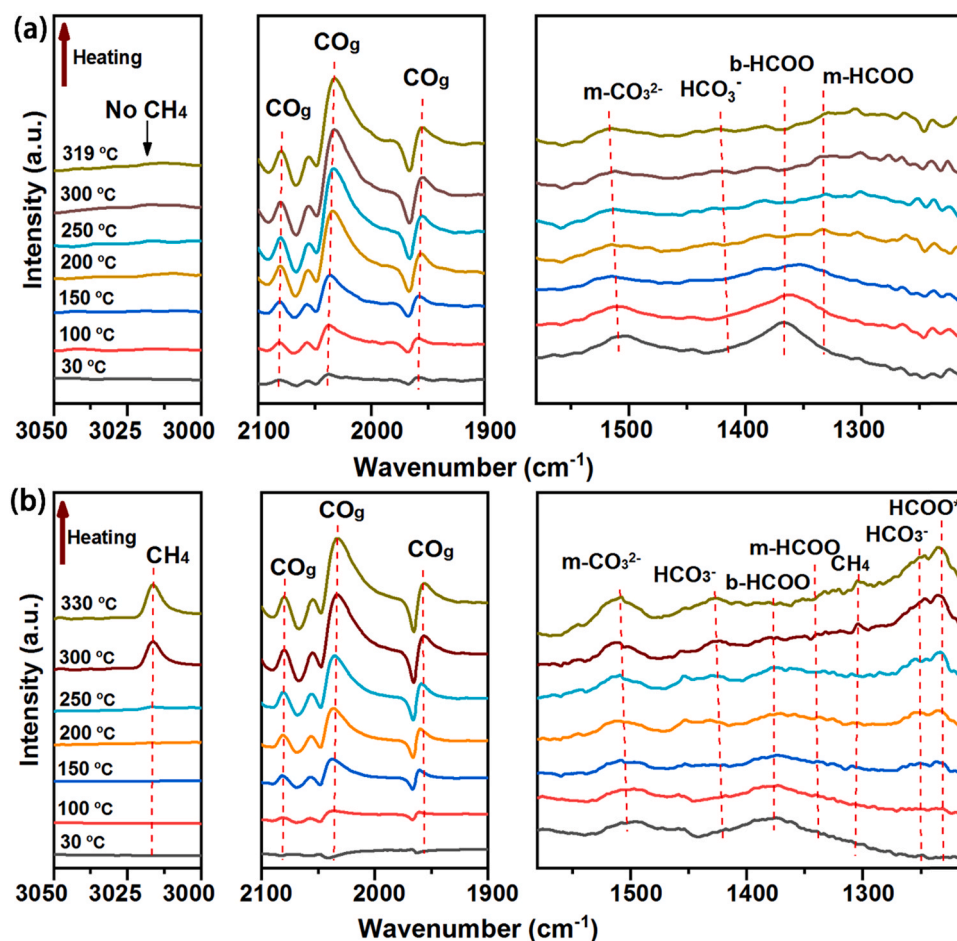
Fig. 6. *In situ* DRIFTS spectra during temperature-programmed reaction of a gas mixture (10 mL/min) containing 10 vol% CO_2, 40 vol% H_2 and 50 vol% He over 8Ni/P25 (a) and 8Ni/TiO_2 (b). The heating rate is 10 °C/min.

at g = 2.003 and also displays an obvious EPR signal at g = 1.985 ascribed to Ti^{3+} species where no signal can be observed for 8Ni/P25 and TiO_2. It verifies more sufficient defects in 8Ni/TiO_2, well in accordance with the results of H_2-TPR and XPS analysis. Surface defects are considered to induce high free electron concentration and serve as the active sites to facilitate the adsorption and activation of CO_2, playing a crucial role in the reaction activity [48,49]. Thereby, CO_2-TPD of 8Ni/P25 (Fig. 5e) displays two peaks at 82 °C and 220 °C, corresponding to the weak and medium surface basic sites, respectively. However, 8Ni/TiO_2 can observe a wider and higher peak in the range of 100–450 °C, which is due to the existence of the strong basic sites. Rich OVs promotes the formation of stronger bonding with more CO_2 molecules on the surface of catalyst. Table S1 The calculated value of CO_2 uptake (Table S1) from CO_2-TPD for 8Ni/TiO_2 achieves at 390 μmol/g_{cat} that is much higher than that of 5Ni/TiO_2 and 10Ni/TiO_2, while the value of 8Ni/P25 shows only 158 μmol/g_{cat}. It further demonstrates the superior ability to adsorb and activate CO_2 on 8Ni/TiO_2. Likewise, H_2-TPD profile of 8Ni/TiO_2 in Fig. 5f shows a stronger signal than that of 8Ni/P25. The H_2 uptake (Table S1) is calculated to be 296 μmol/g_{cat} and 99 μmol/g_{cat} for 8Ni/TiO_2 and 8Ni/P25, respectively, manifesting that more H_2 can be absorbed and activated on 8Ni/TiO_2.

Given the above analysis, it can be deduced that Ni^{2+} enters the lattice of TiO_2 and leads to a strong interaction between Ni-O-Ti in the precursor of 8Ni/TiO_2. During the hydrogen reduction process, Ni species is converted to high-dispersed small-size Ni NPs, leading the formation of Ni-Ov-Ti^{3+}, which is benificial to promote the CO_2 methanation [34, 42]. The formed high-dispersed small-size Ni NPs (from the results of XRD patterns and element mapping) may activate the hydrogen species

that further reduces the part of Ti^{4+} to Ti^{3+} and finally generates more surface defects on TiO_2 [50]. It has been reported that surface defects of reducible oxides (e.g., CeO_2, TiO_2) serve as active sites for CO_2 adsorption to participate in CO_2 methanation process [51].

To gain deep insights into the reason for the different product selectivity between 8Ni/TiO_2 and 8Ni/P25, in situ DRIFTS studies were carried out to determine the CO_2 reaction pathways. IR fingerprint regions of 1200–1500 cm^{-1}, 1900–2100 cm^{-1} and 3000–3050 cm^{-1} are concerned, in which the characteristic peaks of the intermediates are usually observed. The assignments of IR bands of surface-activated species are summarized in Table S3. For the DRIFTS spectra of 8Ni/P25 (Fig. 6a), the key bands at 1375, 1416 and 1510 cm^{-1} assigned to bidentate formate (b-HCOO), bicarbonate (HCO_3^-) and monodentate carbonates (m-CO_3^{2-}) can be observed, respectively. With the temperature raising, the signals for carbonates tails off accompanying with the appearance of the new peak at 1332 cm^{-1} for monodentate formate (m-HCOO) and typical peaks for the linear or bridge CO in the middle range of 1900–2100 cm^{-1}. The DRIFTS spectra of 8Ni/TiO_2 are depicted in Fig. 6b, where the similar peaks at 1332, 1375, 1416, 1510, 1900–2100 cm^{-1} appear and are ascribed to m-HCOO, b-HCOO, HCO_3^-, m-CO_3^{2-}, and CO species, respectively. It infers that CO can be formed on both 8Ni/TiO_2 and 8Ni/P25 and also obeys a same pathway during the reaction. Furthermore, 8Ni/TiO_2 displays the new peaks at 1230 and 1250 cm^{-1} that are diagnostic of the vibrations of COOH* and HCO_3^- species. And also, the obvious peaks at 1304, 3016 cm^{-1} signified the CH_4 formation are observed, which is in accordance with results of the catalytic performance. It is noteworthy that the signal intensity of crucial intermediates for CO_2 methanation formate species and
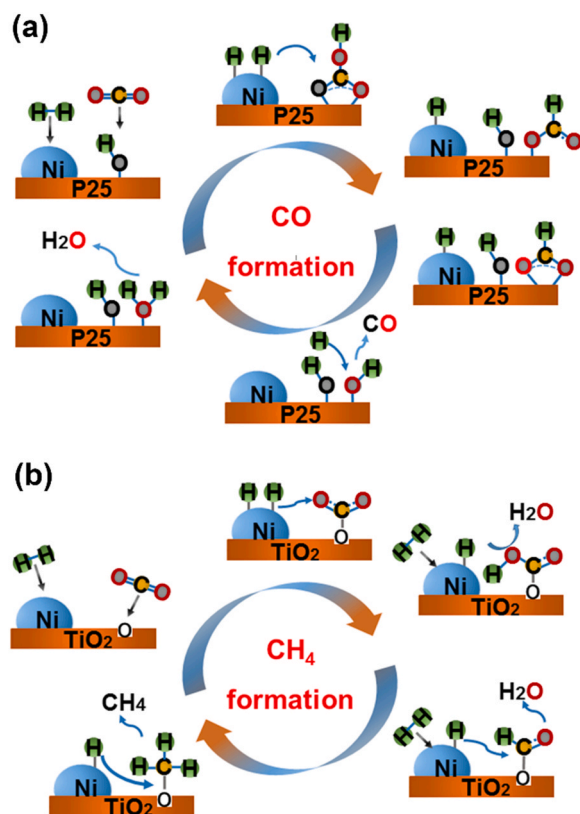
Scheme 1. CO and CH$_4$ formation mechanism.

carbonate species becomes stronger, probably because more exited OVs facilitate the activation of CO$_2$ during the reaction process.

Based on the investigation of in situ DRIFTS, a description of the possible CO$_2$ conversion pathways over 8Ni/P25 and 8Ni/TiO$_2$ is presented in Scheme 1. For the lack of surface defects, 8Ni/P25 only displays a conventional pathway of CO formation as reported [52]. Firstly, atomic hydrogen species generates via the dissociation of H$_2$ on Ni NPs and rapidly diffuses through the overflow process. CO$_2$ molecule is activated by hydroxyl group on the surface of P25 to form carbonate species that can be further reduced by H atom to m-HCOO on P25 and finally rearranges to release CO and H$_2$O. For 8Ni/TiO$_2$, the formation of CH$_4$ dominantly takes place in parallel with CO possibly via a formate-mediated pathway reported by Kattel et al. [53]. Firstly, CO$_2$ molecule can be strongly absorbed by O^{2-} sites to form carbonate species in the whole reaction process. The O^{2-} site is plausibly formed by CO$_2$ chemisorption and dissociation and then inserts into the OVs [54]. Subsequently, more atomic hydrogen species formed on high-dispersed small-sized Ni NPs promotes the conversion of carbonates to formate species that further participates in the transformation to methoxy group and finally generates CH$_4$.

4. Conclusion

In conclusion, this work reported a MOF-template method to prepare xNi/TiO$_2$ catalysts for efficient IR driven CO$_2$ methanation. 8Ni/TiO$_2$ exhibited a maximum CH$_4$ production rate of 463.9 mmol g$_{Ni}^{-1}$ h^{-1} and almost 100% selectivity for CH$_4$ under IR light with 1530 mW/cm^2. Characterizations revealed that enhanced photothermal catalytic performance of 8Ni/TiO$_2$ can be ascribed to homogeneously-distributed and small-size Ni NPs, good adsorption and activation capacity of CO$_2$ and H$_2$, strong IR light absorption and efficient light-to-heat conversion ability. IR light accelerating CO$_2$ methanation over 8Ni/TiO$_2$ was related to a photo-driven thermal catalysis. In comparison to UV–vis or full spectrum light which affected catalytic activity through induced

electron transition, IR served as the optimum light source to offer thermal energy and promote highly efficient photothermal CO$_2$ methanation with higher yield and selectivity of CH$_4$ over 8Ni/TiO$_2$. Moreover, the strong interaction between Ni species and TiO$_2$ promoted the formation of Ti^{3+} and OVs on 8Ni/TiO$_2$, which accounted for the high selectivity of CH$_4$. The CO and CH$_4$ formation pathways over 8Ni/TiO$_2$ and 8Ni/P25 were revealed by in situ DRIFTS studies. Therefore, this work proposed a potential alternative strategy for efficient CO$_2$ reduction and utilization of renewable solar energy via infrared light photothermal catalysis instead of traditional heating mode.

CRediT authorship contribution statement

Qiang Li: Conceptualization, Data curation, Formal analysis, Investigation, Methodology, Resources, Writing – original draft. **Yanxia Gao:** Methodology, Writing – review & editing. **Meng Zhang:** Methodology, Resources. **Hui Gao:** Methodology. **Jing Chen:** Writing – review & editing. **Hongpeng Jia:** Conceptualization, Supervision, Writing – review & editing, Project administration, Funding acquisition.

Declaration of Competing Interest

The authors declare that they have no known competing financial interests or personal relationships that could have appeared to influence the work reported in this paper.

Acknowledgments

Appendix A. Supporting information

Supplementary data associated with this article can be found in the online version at doi:10.1016/j.apcatb.2021.120905.

References

[1] S. Saeidi, S. Najari, V. Hessel, K. Wilson, F.J. Keil, P. Concepción, S.L. Suib, A. E. Rodrigues, Recent advances in CO$_2$ hydrogenation to value-added products-current challenges and future directions, Prog. Energy Combust. Sci. 85 (2021), 100905, https://doi.org/10.1016/j.pecs.2021.100905.
[2] T. Mendiara, F. García-Labiano, A. Abad, P. Gayán, L.F. de Diego, M.T. Izquierdo, J. Adánez, Negative CO$_2$ emissions through the use of biofuels in chemical looping technology: A review, Appl. Energy 232 (2018) 657–684, https://doi.org/10.1016/j.apenergy.2018.09.201.
[3] A.A. Khan, M. Tahir, Recent advancements in engineering approach towards design of photo-reactors for selective photocatalytic CO$_2$ reduction to renewable fuels, J. CO$_2$ Util. 29 (2019) 205–239, https://doi.org/10.1016/j.jcou.2018.12.008.
[4] S. Roy, A. Cherevotan, S.C. Peter, Thermochemical CO$_2$ hydrogenation to single carbon products: Scientific and technological challenges, ACS Energy Lett. 3 (2018) 1938–1966, https://doi.org/10.1021/acsenergylett.8b00740.
[5] V. Golovanova, M.C. Spadaro, J. Arbiol, V. Golovanov, T.T. Rantala, T. Andreu, J. R. Morante, Effects of solar irradiation on thermally driven CO$_2$ methanation using Ni/CeO$_2$-based catalyst, Appl. Catal. B: Environ. 291 (2021) 120038, https://doi.org/10.1016/j.apcatb.2021.120038.
[6] D. Mateo, N. Morlanes, P. Maity, G. Shterk, O.F. Mohammed, J. Gascon, Efficient visible-light driven photothermal conversion of CO$_2$ to methane by nickel nanoparticles supported on barium titanate, Adv. Funct. Mater. 31 (2020), 2008244, https://doi.org/10.1002/adfm.202008244.
[7] J. Zhao, B. Liu, L. Meng, S. He, R. Yuan, Y. Hou, Z. Ding, H. Lin, Z. Zhang, X. Wang, J. Long, Plasmonic control of solar-driven CO$_2$ conversion at the metal/zno interfaces, Appl. Catal. B: Environ. 256 (2019) 117823, https://doi.org/10.1016/j.apcatb.2019.117823.
[8] H. Zhou, P. Li, J. Guo, R. Yan, T. Fan, D. Zhang, J. Ye, Artificial photosynthesis on tree trunk derived alkaline tantalates with hierarchical anatomy: Towards CO$_2$ photo-fixation into CO and CH$_4$, Nanoscale 7 (2015) 113–120, https://doi.org/10.1039/c4nr03019b.

[9] L. Collado, P. Jana, B. Sierra, J.M. Coronado, P. Pizarro, D.P. Serrano, V.A. de la Peña O'Shea, Enhancement of hydrocarbon production via artificial photosynthesis due to synergetic effect of Ag supported on TiO2 and ZnO semiconductors, Chem. Eng. J. 224 (2013) 128–135, https://doi.org/10.1016/j.cej.2012.12.053.

[10] H. Liu, L. Shi, Q. Zhang, P. Qi, Y. Zhao, Q. Meng, X. Feng, H. Wang, J. Ye, Photothermal catalysts for hydrogenation reactions, Chem. Commun. (Camb.) 57 (2021) 1279–1294, https://doi.org/10.1039/d0cc07144g.

[11] W.K. Fan, M. Tahir, Recent developments in photothermal reactors with understanding on the role of light/heat for CO2 hydrogenation to fuels: A review, Chem. Eng. J. 427 (2022), 131617, https://doi.org/10.1016/j.cej.2021.131617.

[12] Z.J. Wang, H. Song, H. Liu, J. Ye, Coupling of solar energy and thermal energy for carbon dioxide reduction: Status and prospects, Angew. Chem. Int. Ed. Engl. 59 (2020) 8016–8035, https://doi.org/10.1002/anie.201907443.

[13] X. Meng, T. Wang, L. Liu, S. Ouyang, P. Li, H. Hu, T. Kako, H. Iwai, A. Tanaka, J. Ye, Photothermal conversion of CO2 into CH4 with H2 over group VIII nanocatalysts: An alternative approach for solar fuel production, Angew. Chem. Int. Ed. Engl. 53 (2014) 11478–11482, https://doi.org/10.1002/anie.201404953.

[14] L. Lin, K. Wang, K. Yang, X. Chen, X. Fu, W. Dai, The visible-light-assisted thermocatalytic methanation of CO2 over Ru/TiO(2−x)Nx, Appl. Catal. B: Environ. 204 (2017) 440–455, https://doi.org/10.1016/j.apcatb.2016.11.054.

[15] P.G. O'Brien, K.K. Ghuman, A.A. Jelle, A. Sandhel, T.E. Wood, J.Y.Y. Loh, J. Jia, D. Perovic, C.V. Singh, N.P. Kherani, C.A. Mims, G.A. Ozin, Enhanced photothermal reduction of gaseous CO2 over silicon photonic crystal supported ruthenium at ambient temperature, Energy Environ. Sci. 11 (2018) 3443–3451, https://doi.org/10.1039/c8ee02347f.

[16] P.G. O'Brien, A. Sandhel, T.E. Wood, A.A. Jelle, L.B. Hoch, D.D. Perovic, C. A. Mims, G.A. Ozin, Photomethanation of gaseous CO2 over Ru/Silicon nanowire catalysts with visible and near-infrared photons, Adv. Sci. 1 (2014), 1400001, https://doi.org/10.1002/advs.201400001.

[17] D. Mateo, J. Albero, H. García, Photoassisted methanation using Cu2O nanoparticles supported on graphene as a photocatalyst, Energy Environ. Sci. 10 (2017) 2392–2400, https://doi.org/10.1039/c7ee02287e.

[18] J.-J. Li, S.-C. Cai, E.-Q. Yu, B. Weng, X. Chen, J. Chen, H.-P. Jia, Y.-J. Xu, Efficient infrared light promoted degradation of volatile organic compounds over photo-thermal responsive Pt-rGO-TiO2 composites, Appl. Catal. B: Environ. 233 (2018) 260–271, https://doi.org/10.1016/j.apcatb.2018.04.011.

[19] X. Chen, Q. Li, M. Zhang, J. Li, S. Cai, J. Chen, H. Jia, MOF-templated preparation of highly dispersed Co/Al2O3 composite as the photothermal catalyst with high solar-to-fuel efficiency for CO2 methanation, ACS Appl. Mater. Interfaces 12 (2020) 39304–39317, https://doi.org/10.1021/acsami.0c11576.

[20] E. Yu, J. Li, J. Chen, J. Chen, Z. Hong, H. Jia, Enhanced photothermal catalytic degradation of toluene by loading Pt nanoparticles on manganese oxide: Photoactivation of lattice oxygen, J. Hazard. Mater. 388 (2020), 121800, https://doi.org/10.1016/j.jhazmat.2019.121800.

[21] J. Xu, Z. Ju, W. Zhang, Y. Pan, J. Zhu, J. Mao, X. Zheng, H. Fu, M. Yuan, H. Chen, R. Li, Efficient infrared-light-driven CO2 reduction over ultrathin metallic Ni-doped CoS2 nanosheets, Angew. Chem. Int. Ed. 60 (2021) 8705–8709, https://doi.org/10.1002/anie.202017041.

[22] X. Li, L. Liang, Y. Sun, J. Xu, X. Jiao, X. Xu, H. Ju, Y. Pan, J. Zhu, Y. Xie, Ultrathin conductor enabling efficient IR light CO2 reduction, J. Am. Chem. Soc. 141 (2019) 423–430, https://doi.org/10.1021/jacs.8b10692.

[23] A. Vita, C. Italiano, L. Pino, P. Frontera, M. Ferraro, V. Antonucci, Activity and stability of powder and monolith-coated Ni/GDC catalysts for CO2 methanation, Appl. Catal. B: Environ. 226 (2018) 384–395, https://doi.org/10.1016/j.apcatb.2017.12.078.

[24] I. Hussain, A.A. Jalil, N.S. Hassan, M.Y.S. Hamid, Recent advances in catalytic systems for CO2 conversion to substitute natural gas (SNG): Perspective and challenges, J. Energy Chem. 62 (2021) 377–407, https://doi.org/10.1016/j.jechem.2021.03.040.

[25] X. Yan, W. Sun, L. Fan, P.N. Duchesne, W. Wang, C. Kubel, D. Wang, S.G.H. Kumar, Y.F. Li, A. Tavasoli, T.E. Wood, D.L.H. Hung, L. Wan, L. Wang, R. Song, J. Guo, I. Gourevich, A.A. Jelle, J. Lu, R. Li, B.D. Hatton, G.A. Ozin, Nickel@siloxene catalytic nanosheets for high-performance CO2 methanation, Nat. Commun. 10 (2019) 2608, https://doi.org/10.1038/s41467-019-10464-x.

[26] Z. Chen, Z. Chen, O.K. Farha, K.W. Chapman, Mechanistic insights into nanoparticle formation from bimetallic metal-organic frameworks, J. Am. Chem. Soc. 143 (2021) 8976–8980, https://doi.org/10.1021/jacs.1c04269.

[27] R.R. Ikreedeegh, M. Tahir, Indirect Z-scheme heterojunction of NH2-MIL-125(Ti) MOF/g-C3N4 nanocomposite with RGO solid electron mediator for efficient photocatalytic CO2 reduction to CO and CH4, J. Environ. Chem. Eng. 9 (2021), 105600, https://doi.org/10.1016/j.jece.2021.105600.

[28] W.K. Fan, M. Tahir, Recent trends in developments of active metals and heterogeneous materials for catalytic CO2 hydrogenation to renewable methane: A review, J. Environ. Chem. Eng. 9 (2021), 105460, https://doi.org/10.1016/j.jece.2021.105460.

[29] M.Z. Hussain, Z. Yang, Z. Huang, Q. Jia, Y. Zhu, Y. Xia, Recent advances in metal-organic frameworks derived nanocomposites for photocatalytic applications in energy and environment, Adv. Sci. 8 (2021), e2100625, https://doi.org/10.1002/advs.202100625.

[30] W.K. Fan, M. Tahir, Current trends and approaches to boost the performance of metal-organic frameworks for carbon dioxide methanation through photo/thermal hydrogenation: A Review, Ind. Eng. Chem. Res. 60 (2021) 13149–13179, https://doi.org/10.1021/acs.iecr.1c02058.

[31] B. Deng, H. Song, K. Peng, Q. Li, J. Ye, Metal-organic framework-derived Ga-Cu/CeO2 catalyst for highly efficient photothermal catalytic CO2 reduction, Appl.

[32] Catal. B: Envirol. 298 (2021), 120519, https://doi.org/10.1016/j.apcatb.2021.120519.

[32] N. Li, X. Liu, J. Zhou, W. Chen, M. Liu, Encapsulating CuO quantum dots in MIL-125(Ti) coupled with g-C3N4 for efficient photocatalytic CO2 reduction, Chem. Eng. J. 399 (2020), 125782, https://doi.org/10.1016/j.cej.2020.125782.

[33] M. Tahir, N.A.S. Amin, Photo-induced CO2 reduction by hydrogen for selective CO evolution in a dynamic monolith photoreactor loaded with Ag-modified TiO2 nanocatalyst, Int. J. Hydrog. Energy 42 (2017) 15507–15522, https://doi.org/10.1016/j.ijhydene.2017.05.039.

[34] Z. Hao, J. Shen, S. Lin, X. Han, X. Chang, J. Liu, M. Li, X. Ma, Decoupling the effect of Ni particle size and surface oxygen deficiencies in CO2 methanation over ceria supported Ni, Appl. Catal. B: Environ. 286 (2021), 119922, https://doi.org/10.1016/j.apcatb.2021.119922.

[35] X. Chen, X. Chen, S. Cai, J. Chen, W. Xu, H. Jia, J. Chen, Catalytic combustion of toluene over mesoporous Cr2O3-supported platinum catalysts prepared by in situ pyrolysis of MOFs, Chem. Eng. J. 334 (2018) 768–779, https://doi.org/10.1016/j.cej.2017.10.091.

[36] X. Chen, X. Chen, S. Cai, E. Yu, J. Chen, H. Jia, MnOx/Cr2O3 composites prepared by pyrolysis of Cr-MOF precursors containing in situ assembly of MnOx as high stable catalyst for toluene oxidation, Appl. Surf. Sci. 475 (2019) 312–324, https://doi.org/10.1016/j.apsusc.2018.12.277.

[37] S. Wu, S. Li, Q. Zhang, Z. Jiang, Y. Yang, J. Wu, X. Zhao, High light-to-fuel efficiency and CO2 reduction rates achieved on a unique nanocomposite of Co/Co doped Al2O3 nanosheets with UV–vis-IR irradiation, Energy Enviro. Sci. 12 (2019) 2581–2590, https://doi.org/10.1039/c9ee01484e.

[38] H. Liu, T.D. Dao, L. Liu, X. Meng, T. Nagao, J. Ye, Light assisted CO2 reduction with methane over group VIII metals: Universality of metal localized surface plasmon resonance in reactant activation, Appl. Catal. B: Enviro. 209 (2017) 183–189, https://doi.org/10.1016/j.apcatb.2017.02.080.

[39] X. Chen, J.-J. Li, X. Chen, S.-C. Cai, E.-Q. Yu, J. Chen, H. Jia, MOF-templated approach for hollow NiOx/Co3O4 catalysts: Enhanced light-driven thermocatalytic degradation of toluene, ACS Appl. Nano Mater. 1 (2018) 2971–2981, https://doi.org/10.1021/acsanm.8b00587.

[40] P. Christopher, H. Xin, A. Marimuthu, S. Linic, Singular characteristics and unique chemical bond activation mechanisms of photocatalytic reactions on plasmonic nanostructures, Nat. Mater. 11 (2012) 1044–1050, https://doi.org/10.1038/nmat3454.

[41] J. Li, Y. Lin, X. Pan, D. Miao, D. Ding, Y. Cui, J. Dong, X. Bao, Enhanced CO2 methanation activity of Ni/anatase catalyst by tuning strong metal-support interactions, ACS Catal. 9 (2019) 6342–6348, https://doi.org/10.1021/acscatal.9b00401.

[42] M. Xu, S. He, H. Chen, G. Cui, L. Zheng, B. Wang, M. Wei, TiO2−x-modified Ni nanocatalyst with tunable metal-support interaction for water–gas shift reaction, ACS Catal. 7 (2017) 7600–7609, https://doi.org/10.1021/acscatal.7b01951.

[43] Y. Lin, Y. Zhu, X. Pan, X. Bao, Modulating the methanation activity of Ni by the crystal phase of TiO2, Catal. Sci. Technol. 7 (2017) 2813–2818, https://doi.org/10.1039/c7cy00124j.

[44] C.-S. Chen, C.S. Budi, H.-C. Wu, D. Saikia, H.-M. Kao, Size-tunable Ni nanoparticles supported on surface-modified, cage-type mesoporous silica as highly active catalysts for CO2 hydrogenation, ACS Catal. 7 (2017) 8367–8381, https://doi.org/10.1021/acscatal.7b02310.

[45] W.L. Vrijburg, E. Moioli, W. Chen, M. Zhang, B.J.P. Terlingen, B. Zijlstra, I.A. W. Filot, A. Züttel, E.A. Pidko, E.J.M. Hensen, Efficient base-metal NiMn/TiO2 catalyst for CO2 methanation, ACS Catal. 9 (2019) 7823–7839, https://doi.org/10.1021/acscatal.9b01968.

[46] A.A. Khan, M. Tahir, Well-designed 2D/2D Ti3C2TA/R MXene coupled g-C3N4 heterojunction with in-situ growth of anatase/rutile TiO2 nucleates to boost photocatalytic dry-reforming of methane (DRM) for syngas production under visible light, Appl. Catal. B: Environ. 285 (2021), 119777, https://doi.org/10.1016/j.apcatb.2020.119777.

[47] J.J. Li, B. Weng, S.C. Cai, J. Chen, H.P. Jia, Y.J. Xu, Efficient promotion of charge transfer and separation in hydrogenated TiO2/WO3 with rich surface-oxygen-vacancies for photodecomposition of gaseous toluene, J. Hazard. Mater. 342 (2018) 661–669, https://doi.org/10.1016/j.jhazmat.2017.08.077.

[48] R. Shi, Y. Chen, Controlled formation of defective shell on TiO2 (001) facets for enhanced photocatalytic CO2 reduction, ChemCatChem 11 (2019) 2270–2276, https://doi.org/10.1002/cctc.201900061.

[49] S.A. Rawool, K.K. Yadav, V. Polshettiwar, Defective TiO2 for photocatalytic CO2 conversion to fuels and chemicals, Chem. Sci. 12 (2021) 4267–4299, https://doi.org/10.1039/d0sc06451c.

[50] Z.G.Mi Xiong, Yong Qin, Spillover in heterogeneous catalysis: new insights and opportunities, ACS Catal. 11 (2021) 3159–3172, https://doi.org/10.1021/acscatal.0c05567.

[51] L. Shen, J. Xu, M. Zhu, Y.-F. Han, Essential role of the support for nickel-based CO2 methanation catalysts, ACS Catal. 10 (2020) 14581–14591, https://doi.org/10.1021/acscatal.0c03471.

[52] J. Jia, P.G. O'Brien, L. He, Q. Qiao, T. Fei, L.M. Reyes, T.E. Burrow, Y. Dong, K. Liao, M. Varela, S.J. Pennycook, M. Hmadeh, A.S. Helmy, N.P. Kherani, D. D. Perovic, G.A. Ozin, Visible and near-infrared photothermal catalyzed hydrogenation of gaseous CO2 over nanostructured Pd@Nb2O5, Adv. Sci. 3 (2016), 1600189, https://doi.org/10.1002/advs.201600189.

[53] S. Kattel, P. Liu, J.G. Chen, Tuning selectivity of CO2 hydrogenation reactions at the metal/oxide interface, J. Am. Chem. Soc. 139 (2017) 9739–9754, https://doi.org/10.1021/jacs.7b05362.

[54] A. Westermann, B. Azambre, M.C. Bacariza, I. Graça, M.F. Ribeiro, J.M. Lopes, C. Henriques, Insight into CO2 methanation mechanism over NiUSY zeolites: An

operando IR study, Appl. Catal. B: Environ. 174–175 (2015) 120–125, https://doi.org/10.1016/j.apcatb.2015.02.026.